# Titanium dioxide and table sugar enhance the leaching of silver out of nanosilver packaging

**Tianxi Yang[1†‡], Laxmi Adhikari[1‡],Teena Paulose[2], Reiner Bleher[3], and Timothy V. Duncan[1*]**

[1]Center for Food Safety and Nutrition, US Food and Drug Administration, Bedford Park IL, 60501

[2]Department of Food Science and Nutrition, Illinois Institute of Technology, Bedford Park IL, 60501

[3]Department of Materials Science and Engineering and the Northwestern University Atomic and Nanoscale Characterization Experimental (NUANCE) Center, Northwestern University, Evanston, IL 60208

[†]Current affiliation: Food Nutrition and Health Program, Faculty of Land and Food Systems, University of British Columbia, Vancouver, BC V6T 1Z4, Canada

[‡]Contributed equally to this work

*Author to whom correspondence should be addressed: timothy.duncan@fda.hhs.gov

# Supporting information

## Supplementary Materials and Methods

**Raman analysis of $TiO_2$ particles**. Raman analysis of micro- or nanocrystalline $TiO_2$ particles was performed using a Horiba XploRA PLUS Raman spectrometer, equipped with a 532 nm laser and 10× objective lens. Powders were dispersed in water at 0.05 wt % and then ~25 µL was dropped on glass microscope slides coated with aluminum foil and allowed to dry. Raman spectra were acquired with a 600 gr/mm grating, 10 s acquisition time, and a 50% ($nTiO_2$) or 10% ($\mu TiO_2$) intensity filter. The collected spectra were processed to remove baseline using Labspec 6 software. Spectra are the average of 10 repeated acquisitions.

**Darkfield microscopy.** Darkfield microscope images of $nTiO_2$ and $\mu TiO_2$ (**Figure 1**) were acquired on an Olympus DSX-510i inverted digital microscope using a 50× objective (Olympus, MPLFLN50XBDP) in darkfield mode. The images were captured with a 1× optical

zoom (total magnification 693×), using the instrument's enhanced focal imaging (EFI) mode and an exposure time of 0.33 ms. Prior to imaging, $TiO_2$ was dispersed in water at 0.05 wt %, briefly vortexed, and stored under ambient light at 40 °C for 4 hours. A small aliquot (20 uL) was removed, diluted 10-fold, and then 20 μL of the diluted dispersion was dropped on a microscope slide and left to dry before imaging.

**X-ray Diffraction (XRD) analysis of $TiO_2$ particles.** XRD was performed on a Brüker D2 Phaser using a copper anode (0.154184 nm wavelength) as X-ray source. $TiO_2$ powder (micro- or nanocrystalline) was loosely added to a rear-mounted sample holder and scraped flush to the holder surface with the edge of a glass microscope slide. A 2 mm air scattering screen, 1 mm divergence slit, and 8 mm detector slit were used to minimize scattering interference from the X-ray source. Samples were rotated at 15 rpm during measurement, and data were acquired with a 2 s integration time over a 2θ angular range of 20-80 degrees. In the case of $TiO_2$ residues after treatment with 0.5 mM $Ag^+$ for 10 days, the $TiO_2$ residues were each deposited on 1 mm thick polished low background silicon wafers, which were then inserted into a rear-mounted sample holder. XRD data on these samples were measured using the same slit hardware and acquisition parameters as the pure $TiO_2$ powders. Small post-hoc adjustments to the scattering angle axis were frequently necessary to account for slight changes in sample height; in such cases, the (110) scattering peak of pure $TiO_2$ was used as a frame of reference. Raw data were processed using the Brüker D2 phaser DIFFRAC.EVA software to subtract the baselines and remove the Cu Kα scattering contributions using automated software functions, after which the data were transferred to OriginLab 2022 software for analysis and plotting.

**UV-Visible Spectroscopy.** UV-Visible spectra of aqueous solutions containing unbound AgNPs were acquired on a Lambda 35 UV-Visible Spectrophotometer (Perkin Elmer). Solutions were added without dilution to 1 cm pathlength, 4 mL volume disposable polypropylene cuvettes (Sarstedt) and immediately scanned at 480 nm/min over a range of 330-800 nm with 1 nm slits. Solutions in water were measured against a pure water blank and those in 9 wt % aqueous sucrose solution were measured against a 9 wt % aqueous sucrose blank. $TiO_2$ particle stability measurements were performed on the same instrument with the same method, except the software was instructed to repeat the measurement every 30 minutes for 24 hrs.

**$TiO_2$ stability measurements in water and sucrose solution.** Aqueous dispersions of 0.05 wt % micro- or nanocrystalline $TiO_2$ in water or 9 wt % sucrose solution were prepared in 15 mL plastic centrifuge tubes (VWR International). The dispersions were vortexed for 30 seconds and immediately transferred to disposable polypropylene cuvettes (4 mL volume, 1 cm pathlength, Sarstedt) and UV-Visible spectra were acquired as described in the previous selection. Measurements were repeated every 30 min for 24 h without disturbing the samples. Photographs were acquired using a Samsung S22 smart phone camera before the first measurement and after the last measurement to demonstrate $TiO_2$ particle settling. Settling kinetics were quantified by recording the optical density of the $TiO_2$ dispersions at 500 nm at each time point. The poor colloidal stability of microcrystalline $TiO_2$ required a brief (few minutes) sonication of these samples in a bath sonicator (Bransonic 2510R 100W ultrasonic bath cleaner) to accurately characterize differences in settling kinetics between water and sucrose. The results of this experiment are displayed in **Figure S3**.

**Dynamic light scattering (DLS) analysis of $TiO_2$ particles.** Hydrodynamic diameters, polydispersities, and zeta-potentials were measured on a Malvern Panalytical Zetasizer Nano ZS. For the experiment shown in **Figure S1**, micro- or nanocrystalline $TiO_2$ particles were dispersed in purified water or 9 wt % aqueous sucrose at 0.05 wt % and sonicated in a bath sonicator (see above) for 5 min. Solutions were then diluted 1:100 (with water or 9 wt % sucrose solution, as appropriate) and immediately transferred to 1 cm plastic sizing cuvettes using a glass pipette. Solvent viscosities, substrate refractive indexes, and other relevant parameters were calculated by the instrument software (Malvern Zetasizer Software v 6.34). Three sequential size measurements were recorded at 173° backscatter after an initial 120 s equilibration time at 25 °C, without disturbing the sample between measurements. $Z_{avg}$ weighted intensity values and polydispersity indices were recorded, and the three replicates were averaged. For zeta-potential measurements, a similar sample preparation protocol was used except the samples were placed via syringe into disposable folded capillary cells. Zeta potential data were measured at 13° forward scattering and processed using a Smoluchowski model in the Zetasizer instrument software. In the experiment shown in **Figure S2**, 0.05 wt % of $nTiO_2$ dispersions in either water or 9 wt % aqueous sucrose solution were prepared, vortexed for 30 s in a bath sonicator (see above), and then immediately transferred to 1 cm sizing cuvettes using a glass pipette. After a 2

min equilibration time at 25 °C, the samples were then measured in sizing mode at 173° backscatter angle every 30 min over a period of 18 h without disturbing the instrument.

**Electron Microscopy**. Electron microscopy of bare μ$TiO_2$ particles used in the simulants and AgNPs used for manufacturing polymer composites was performed on a Hitachi HD-2300 Scanning Tunneling Electron Microscope (STEM) at 200 kV. $TiO_2$ particles after exposure to 500 μM $Ag^+$ for 4 h and 24 h were analyzed by collecting 200 μL aliquots of the test solutions, isolating and washing the precipitate by centrifugation, resuspending in 200 μL water, and drop-casting 8 μL of the suspension on a 200 mesh C-coated Cu grid (Ted Pella, Redding, CA). Images of AgNPs adsorbed to $TiO_2$ particles were recorded with a JEOL Tunneling Electron Microscope (TEM) 1230 at 120kV acceleration voltage. EDS analysis was performed with the Hitachi HD2300 STEM at 200 kV acceleration voltage with a dual EDS system using the Pathfinder software (Thermo Fisher Scientific). All electron microscopy equipment used in this study is located at the BioCryo Facility of NUANCE at Northwestern University (Evanston, IL).

**Synthesis of AgNPs.** Hydrophobic AgNPs capable of being incorporated within LPDE were synthesized in water and phase transferred to chloroform using our published method.[1] Briefly: 90 mL ultrapure water, trisodium citrate dihydrate (100 mM, 5 mL), tannic acid (0.25 mM, 5 mL), and a magnetic stir bar were added into a 250 mL glass Erlenmeyer flask that was placed into a 120 °C oil bath. The flask was heated under vigorous stirring for 15 min. $AgNO_3$ (1 mL, 25 mM) was then injected into the boiling solution. After 15 min, the boiling solution became bright yellow. The resultant AgNP suspension was removed from the oil bath and cooled to room temperature. Excess tannic acid in the suspension was removed by centrifugation (14000 rpm/20598 rcf, 20 min). AgNP concentration was normalized with UV−Vis spectroscopy (the peak maximum at 402 nm reached an absorbance value of 0.55 ± 0.02) after redispersing AgNPs into purified water. Dispersed hydrophilic AgNPs were stored in the refrigerator until further use. To prepare hydrophobic AgNPs, hydrophilic AgNPs were capped with PEG-2000-SH (PEG-thiol, average Mn 2,000). 8 mL of the aqueous AgNP suspension was mixed with 10 mL of PEG-2000-SH aqueous solution (16 mg/mL) in a glass vial and the mixture was vortexed for 1 min and then stored in refrigerator overnight. After that, 10 mL of chloroform was added into the glass vial. After 5 min of shaking, AgNPs capped with PEG-2000-SH had transferred from the

aqueous phase into the chloroform phase. After removing the aqueous layer, hydrophobic AgNPs were collected and sonicated (see above) for 1 min before use.

**Manufacture of AgNP/LDPE films**. Hydrophobic AgNPs were dispersed into LDPE using a DSM Xplore 15 mL micro-compounder. The micro-compounder is a conical co-rotating twin-screw extruder fitted with a 65 mm cast film extrusion die and all processing was performed under a bed of dry nitrogen (flow rate 10 L/min) to minimize polymer and AgNP oxidation. AgNP/LDPE films were prepared using a two-stage masterbatch process. To prepare the first stage masterbatch, the flow screws and mixing barrel were first heated to 150 °C and when the heating blocks were equilibrated, the screw speed was set to speed control mode at 120 rpm with a maximum force tolerance value of 5000 N. Then, 6 g of neat LDPE pellets were added into the mixing chamber using a feed hopper and processed for 2 min. After that, the screw speed was set to zero rpm and 4 mL of as-synthesized hydrophobic AgNPs were added into the chamber drop-wise with a transfer pipette. 6 g of neat LDPE pellets was then added. The screw speed was increased to 120 rpm and the AgNP/LDPE mixture was processed for 10 min. The screw speed was then reduced to 30 rpm, and the melt was extruded as a strand and cut into small pellets. The remaining melt in the chamber was also collected and cut into small pellets. All AgNP/LDPE pellets were dried in a vacuum oven at 40 °C overnight to remove residual solvent. To prepare the AgNP/LDPE film, the cast film extrusion die was first attached to the exit channel of the micro-compounder, and the micro-compounder and the die were heated to 150 °C. After the heating blocks were equilibrated, the screw speed was set at 120 rpm with a speed control mode at 5000 N. 9.5 g of AgNP/LDPE pellets and 2.5 g of neat LDPE pellets were mixed, and the mixture was added into the chamber using the feed hopper and processed for 10 min. The screw control was changed to force control mode at 550 N before extruding the film. The speed (rpm) controlled and torque-controlled rollers of the cast film extrusion die were set to values of 450 rpm and 27 N·m, respectively. The polymer melt exiting the film die was pulled with tweezers and guided on to the rollers for spooling. The polymer melt exiting the film die was cooled with an air-knife set to a flow rate of 20 L $min^{-1}$. Films typically had thicknesses measuring 40 ± 4 μm.

**Characterization of sucrose-$TiO_2$ binding interactions.** Sucrose-$TiO_2$ binding interactions were confirmed by thermogravimetric analysis (TGA) and Raman microscopy. These results are plotted in **Figure S17** and **Figure S18**, respectively. To confirm binding of

sucrose to $TiO_2$ surfaces, 50 mg $nTiO_2$ was dispersed at 0.1 wt% in either purified water, 1 wt % aqueous sucrose solution, or 9 wt % aqueous sucrose solution. All solutions were sonicated for 5 min in a bath sonicator (see above) then stored in an Thermo Max Q4000 orbital shaker set to 60 RPM at 40 °C for approximately 24 h. The precipitates were then each isolated by centrifugation at 3900 rpm (3214 rcf) for 10 min. The supernatants were completely removed by pipette and the residues were taken up in 15 mL purified water and shaken vigorously to mix. The mixtures were centrifuged under the same conditions as above, the supernatants were removed again, and then the washing procedure was repeated. The final residues were then dried under vacuum for 24 h at room temperature. This process was then repeated using $\mu TiO_2$.

For TGA, around 25 mg of each residue was transferred to a tared, platinum TGA pan and analyzed using a TA Instruments Q500 Thermogravimetric Analyzer. Samples were heated at a rate of 10 °C/min from ambient temperature to 600 °C under nitrogen and then from 600 °C to 700 °C at the same rate under air. Samples of fresh (straight from the bottle) $TiO_2$ and crystalline sucrose were also examined.

For Raman microscopy of the $nTiO_2$ specimens, approximately 1 mg of each residue was pressed flat onto a standard glass microscope slide wrapped with aluminum foil. Samples were assayed with the same Raman microscope described above using 532 nm laser excitation, a 1200 gr/mm grating, and a 10× microscope objective. The number of acquisitions and time per acquisition were selected based on the measured intensity, but typical values were 5-15 acquisitions with 30 s per acquisition. The 1000-2000 $cm^{-1}$ spectral range was typically probed with a 10% laser power setting and the 2600-3900 $cm^{-1}$ spectral range was typically probed with a 25% laser power setting. In all cases, 3-4 spots were scanned to make sure the reported results were representative of the sample. In addition to fresh $nTiO_2$ and crystalline sucrose samples, a hydrated sucrose sample (sucrose containing residual bound water) was also examined. Hydrated sucrose was prepared by dropping 25 μL of a 9 wt % aqueous sucrose solution onto a glass microscope slide covered with aluminum foil and allowing the slide to sit undisturbed just until visually dry (around 4-6 h).

## Supplementary Results and Discussion

**Sucrose-$TiO_2$ binding interactions: thermogravimetric analysis (TGA).** TGA data for fresh $TiO_2$, $TiO_2$ incubated in purified water, and $TiO_2$ incubated in aqueous sucrose solution are shown in **Figure S17**. Data for pure crystalline sucrose are also shown for comparison.

In the case of $nTiO_2$ stored in water, the TGA (**Figure S17A**) and derivative TGA (**Figure S17B**) curves show small mass loss events in the region 30-50 °C and 150-200 °C, consistent with loss of surface-adsorbed atmospheric gas (probably $CO_2$) and surface-bound water, respectively. The analogous curves for fresh $nTiO_2$ were nearly identical except for slightly more mass loss associated with adsorbed gas in the 30-50 °C region for the fresh $nTiO_2$.

$nTiO_2$ stored in the presence of 9 wt % sucrose exhibited two new mass loss peaks centered at 295 °C and 410 °C, which can only be due to the decomposition of surface-adsorbed sucrose. $nTiO_2$ incubated with 9 wt % sucrose also featured suppressed mass loss due to bound water, particularly when the sucrose concentration was 9 wt %. The 295 °C mass loss peak for $nTiO_2$ incubated in 9 wt % sucrose solution is a close match to the primary mass loss event of pure sucrose at 288 °C, whereas the 410 °C event is unique to the sucrose-$nTiO_2$ complex. We interpret this to mean that sucrose forms both weak (physisorbed) and strong (chemisorbed) interactions with the $nTiO_2$ surface; the strong $nTiO_2$-sucrose interactions provide significant thermal stabilization of sucrose, as evidenced by the much higher onset of thermal degradation.

The observation of mass loss peaks due to sucrose bound at the surface of $TiO_2$ was reproducible using lower (1 wt %) sucrose concentration and nanocrystalline versus microcrystalline $TiO_2$. Note that the tendency of sucrose to form both strongly and weakly-bound coronal layers on the $TiO_2$ surface has been independently observed by Qiaorun et al[2] using quartz crystal microbalance measurements. For $\mu TiO_2$, the amount of mass loss due to sucrose binding is considerably less than in $nTiO_2$, in agreement with $\mu TiO_2$'s lower available specific surface area. Nevertheless, the primary mass loss peak due to bound sucrose is still evident above the background noise (**Figure S17D**).

**Sucrose-$TiO_2$ binding interactions: Raman spectroscopy.** Raman spectroscopy confirmed the sucrose-$TiO_2$ binding interactions indicated by the TGA results. These results are

shown in **Figure S18**. Due to the strong scattering of $TiO_2$ at Raman shift values < 1300 $cm^{-1}$ (see, e.g., **Figure 1**), we focused primarily on the 1200-1700 $cm^{-1}$ (**Figure S18A**) and 2700-3600 $cm^{-1}$ (**Figures S18B**) regions, where $TiO_2$ features much weaker scattering peaks arising from OH bending and stretching vibrations, respectively, associated with adsorbed water molecules.

In the 1200-1700 $cm^{-1}$ region, the Raman spectrum of $nTiO_2$ incubated with 9 wt % sucrose shows four distinct peaks protruding from the much stronger OH bending vibration band (i-iv, **Figure S18A** blue line marked long acquisition). These peaks are similar to those observed in the Raman spectrum of hydrated sucrose (**Figure S18A**, pink line), implying the presence of sucrose in the n $TiO_2$ residue. In aqueous sucrose solution, Mathlouthi[3] formally assigns these peaks to (i) $CH_2$ scissoring ($\delta$-$CH_2$, 1455 $cm^{-1}$), (ii) $CH_2$ wagging ($\omega$-$CH_2$, 1366 $cm^{-1}$), (ii) $CH_2$ rocking ($\rho$-$CH_2$, 1340 $cm^{-1}$), and (iv) $CH_2$ twisting ($\tau$-$CH_2$, 1260 $cm^{-1}$) motions. (Note that broadening of the transitions due to hydration obscures many weaker peaks evident in Raman spectra of crystalline sucrose[4]; Mathlouthi's assignments only reflect the major contributors to the intensity of each peak.) Although the $CH_2$ bending vibrations in the $nTiO_2$ spectrum have a similar pattern to those observed with pure hydrated sucrose, the transitions are significantly shifted ($\Delta\nu$ = 2, 38, 42, and 67 $cm^{-1}$ for bands i, ii, iii, and iv, respectively). Because the $CH_2$ bending vibrations of sucrose are highly sensitive to hydrogen bonding effects (due to their proximity to the $CH_2OH$ groups), the frequency shifting in the 9 wt% sucrose/$nTiO_2$ Raman spectra is direct evidence that the sucrose in these samples exhibits strong interactions with the $nTiO_2$ surface. The 9% sucrose/$nTiO_2$ spectrum also shows several additional sharp peaks in the $CH_2$ stretching region that are not present in the hydrated sucrose spectrum (marked by * in **Figure S18A**). These are possibly due to sucrose molecules that are more strongly bound to the $TiO_2$ surface and therefore manifest less variability in their structural orientations with respect to other nearby molecules. (Contributions due to bound carbon dioxide may also be indicated in this region.) Such a pseudocrystalline, tightly bound sucrose layer would likely exhibit significantly different thermodynamic stability compared to more loosely bound sucrose-hydrate complexes, which may explain the two distinct thermal degradation peaks in the TGA curves of $nTiO_2$ stored in the presence of sucrose (**Figure S17B**).

In the 2700-3600 $cm^{-1}$ region, the fresh $nTiO_2$ Raman spectrum is dominated by the inhomogeneously broadened scattering band linked to OH stretching vibrations of water

molecules interacting with the $nTiO_2$ surface (**Figure S18B**). Previous Raman investigations of $TiO_2$ define two general classes of $TiO_2$-bound water: chemisorbed (strongly bound) water polymerized by hydrogen bonding on the crystalline faces of $TiO_2$ and physisorbed water that is more amorphous in structure and exhibits a wider range of intermolecular interaction strengths.[5] The most strongly bound water molecules exhibit discrete OH stretching features in the region 3500-3600 $cm^{-1}$ consistent with decreased hydrogen bonding character (region ii)[6]; OH stretch vibrations of the remaining chemisorbed water molecules are shifted to lower frequencies, generally 3400-3500 $cm^{-1}$ (region iii), while the most weakly bound physisorbed water layers exhibit OH stretching frequencies that are more closely reminiscent of bulk water, 3100-3300 $cm^{-1}$ (iv).[7] An additional sharp feature at ~3700 $cm^{-1}$ corresponds to free (not hydrogen-bonded) OH defects on the $TiO_2$ surface (peak i).[8] In our investigation, the Raman spectrum in the OH stretch region of $nTiO_2$ incubated with water is very similar to that of fresh $nTiO_2$ except additional scattering intensity in the 3100-3300 $cm^{-1}$ range (iv), suggesting that the incubation with water gives rise to additional weakly bound water on the $nTiO_2$ surface. In contrast, $nTiO_2$ stored with 9 wt % sucrose features less prominent Raman scattering in region (iv) and the appearance of large scattering peaks around 2800-3000 $cm^{-1}$ (region v), which is where CH and $CH_2$ stretching vibrations (symmetric and asymmetric) typically show up. The CH and $CH_2$ stretching frequencies are also shifted for $nTiO_2$-bound sucrose compared to those of free hydrated sucrose and exhibit better defined structure. Most importantly, the Raman spectra of $nTiO_2$ incubated with sucrose no longer show the sharp peak at 3700 $cm^{-1}$ (i) indicating loss of free OH surface defects when sucrose is bound to $nTiO_2$. Combined, the Raman data support the conclusion that a portion of the sucrose is strongly bound to dangling OH groups and other defect sites on the $nTiO_2$ surface, consistent with the TGA results described above.

Note that when the sucrose content was reduced from 9 wt % to 1 wt %, a concomitant decrease in the intensity of the $CH/CH_2$ stretching vibrations was observed (**Figure 18B**, red line). Shifting of the vibration frequencies was noted as well. Because $nTiO_2$ stored with 1% sucrose solution also had more surface-adsorbed water (see TGA results), this result may imply a complex relationship between the adsorbed sucrose concentration, adsorbed water concentration, and sucrose-water-$nTiO_2$ spatial arrangement in the binding zone that strongly influences the nature of the CH and $CH_2$ vibrational frequencies as well as the thermal stability of the bound sucrose (see, e.g., the different mass loss peak positions of sucrose when the $nTiO_2$ was stored in

9 wt % aqueous sucrose versus 1 wt% sucrose, **Figure S17B**). In a study of glucose/$TiO_2$ binding characteristics, Kim et al observed a dependence of sentinel vibrational frequencies and relative peak intensities on the glucose concentration and implied that the effect may be due to a shift between monodentate and bidentate glucose-$TiO_2$ binding modes.[9] Additional work would be required to fully understand these effects in our system, but the data nevertheless show that sucrose strongly interacts with the $nTiO_2$ surface regardless of the sucrose concentration, and those interactions can have strong implications for the macroscopic properties of both $nTiO_2$ and $\mu TiO_2$ when dispersed in water.

## Supplementary Figures

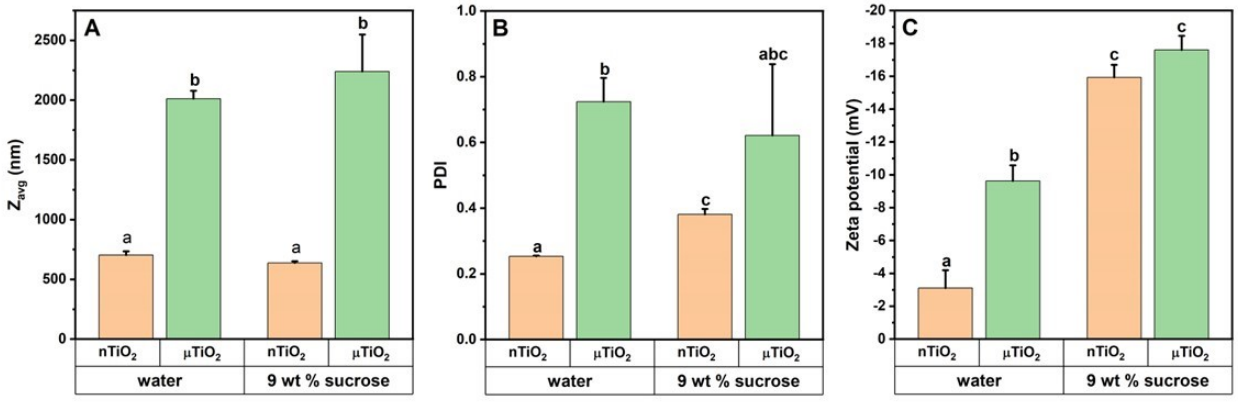


**Figure S1.** Hydrodynamic diameters (A), polydispersity indices (B), and zeta potentials (C) of $nTiO_2$ and $\mu TiO_2$ in both water and 9 wt % aqueous sucrose solution, as measured by dynamic light scattering immediately after dispersion and sonication for 60 s. Each value is the average of three consecutive replicates and the error bars represent standard deviations from the mean. Bars marked by the same letters are not significantly different ($p > 0.05$) from each other. The $TiO_2$ concentration was $5\times10^{-4}$ wt %.

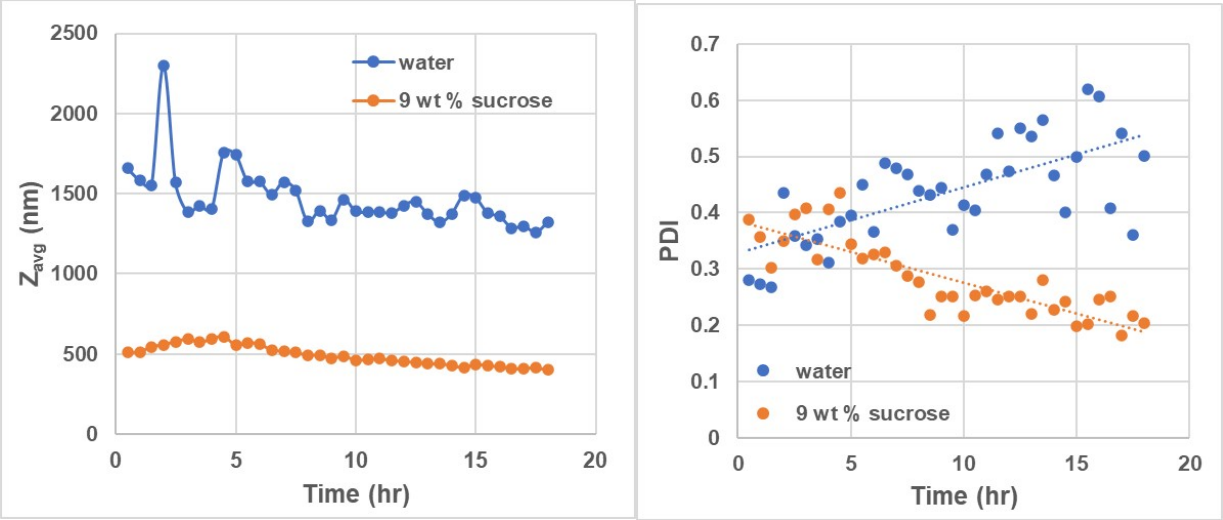


**Figure S2.** Hydrodynamic diameters ($Z_{avg}$, left panel) and polydispersity indices (PDI, right panel) of 0.05 wt % $nTiO_2$ dispersed in water and 9 wt % aqueous sucrose solution as a function of time after preparation at 25 °C. The dashed lines in the right panel indicate linear regressions of the data and are meant to guide the eye. All samples were vortexed for 30 s before the first measurement.

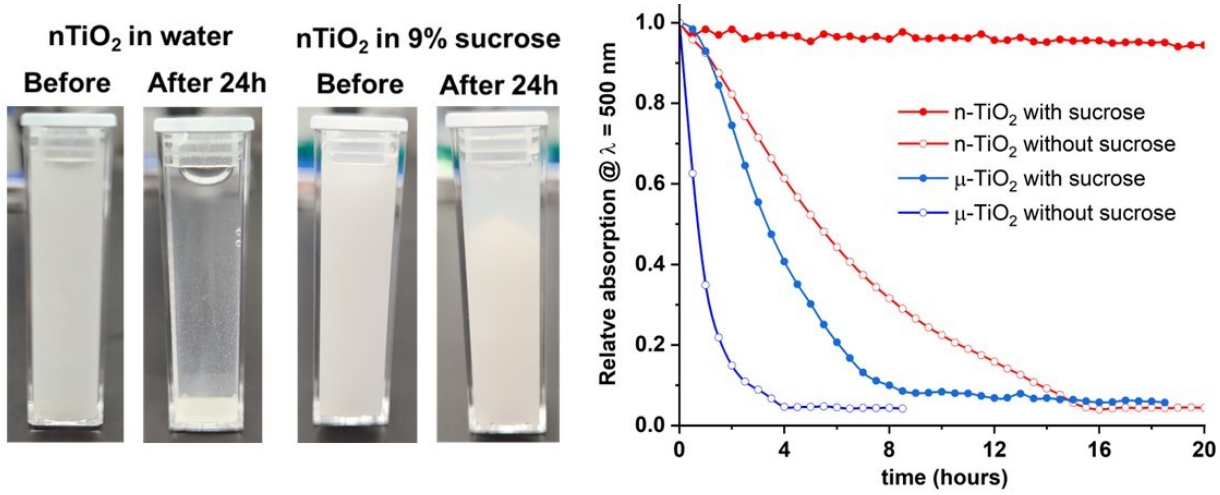


**Figure S3.** (*Left*) Photographs of 0.05 wt % $nTiO_2$ dispersions in water and 9 wt % aqueous sucrose solution immediately after preparation and after 24 hours without mixing or agitation. The dispersion in water is mostly settled. (*Right*) Optical density, measured at 500 nm, of 0.05 wt % $nTiO_2$ (red) and $\mu TiO_2$ (blue) dispersions in either water (open circles) or 9 wt % sucrose solution (closed circles) as a function of time after preparation. Samples were not disturbed during the settling experiment.

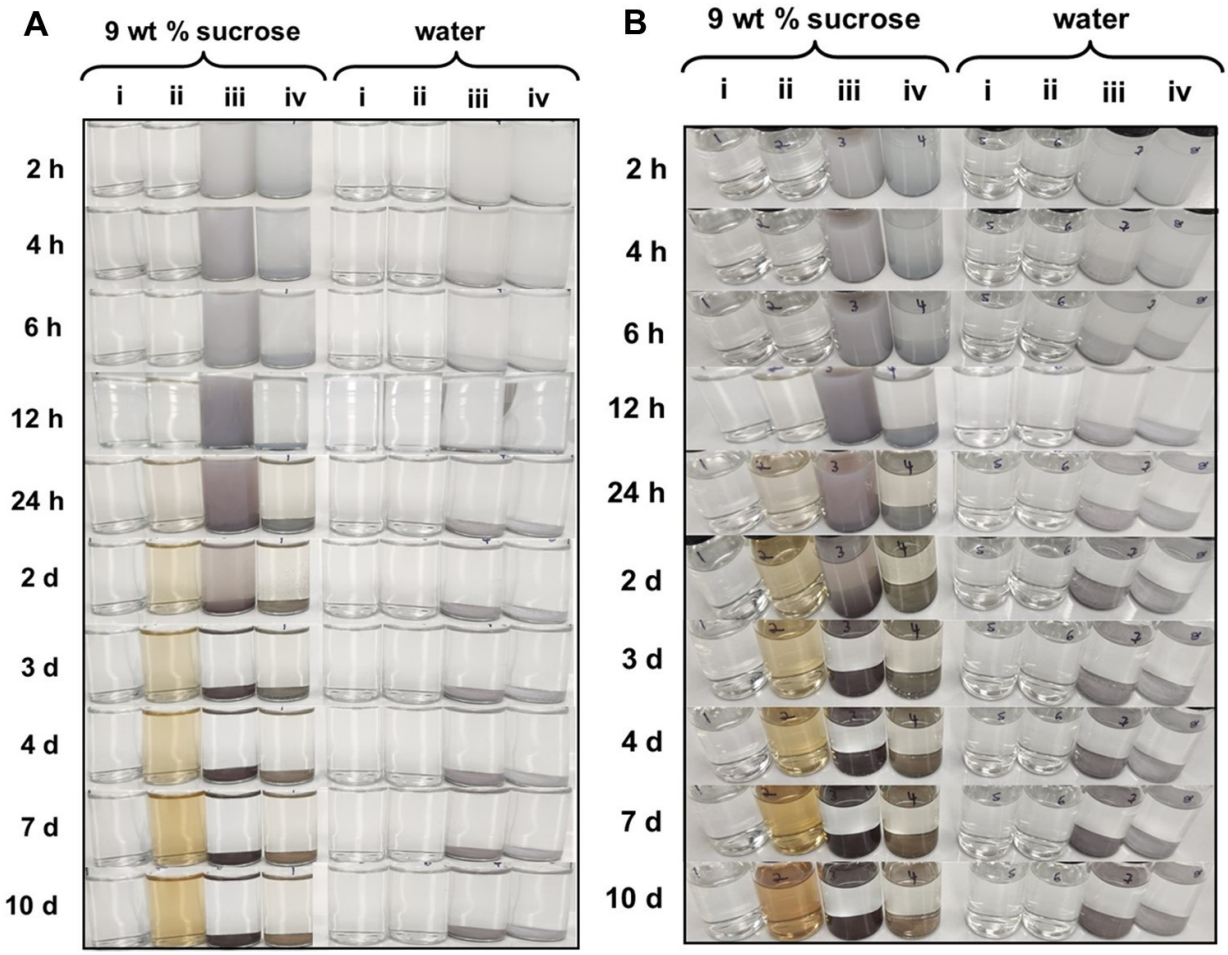


**Figure S4.** Photographs of 0.05 wt % $TiO_2$ dispersions in 9 wt % sucrose and purified water as a function of storage time under ambient light at 40 °C: (i) solvent control (no $TiO_2$ or Ag), (ii) $Ag^+$ but no $TiO_2$, (iii) $Ag^+$ and $nTiO_2$, (iv) $Ag^+$ and $\mu TiO_2$. The $Ag^+$ concentration of 500 μM. These are the same vials as those as those displayed in **Figure 2A** in the main text, except the photographs here were taken before the vials were briefly mixed and those in **Figure 2A** were taken after mixing to disperse the precipitates. Panels (A) and (B) show side-on and top-down viewing angles, respectively. Note the loss of colloidal stability after 12-24 h storage time, even in sucrose-containing dispersions.

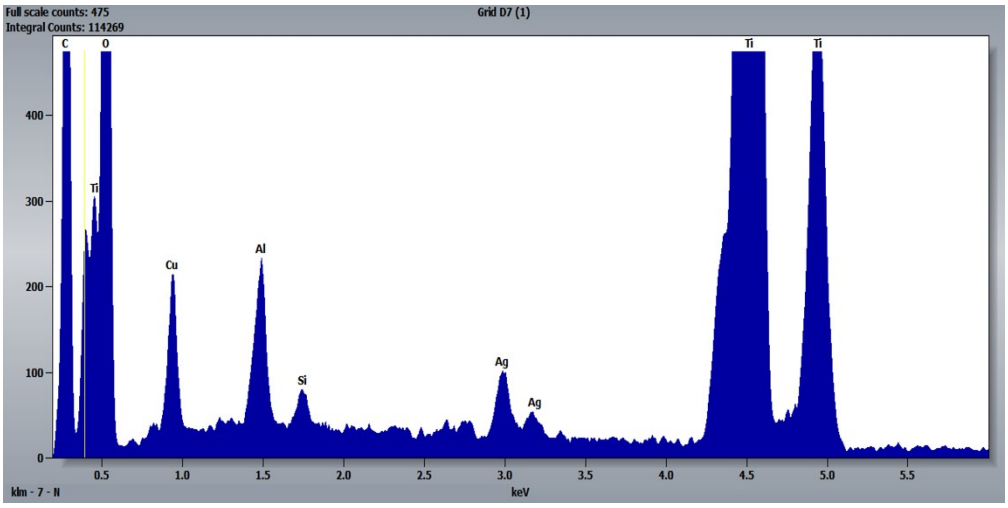


**Figure S5**. Representative EDS spectrum of $nTIO_2$ particles stored with 500 μM $Ag^+$ in 9 wt % sucrose solution for 24 hours. Note the metallic Ag peaks indicated.

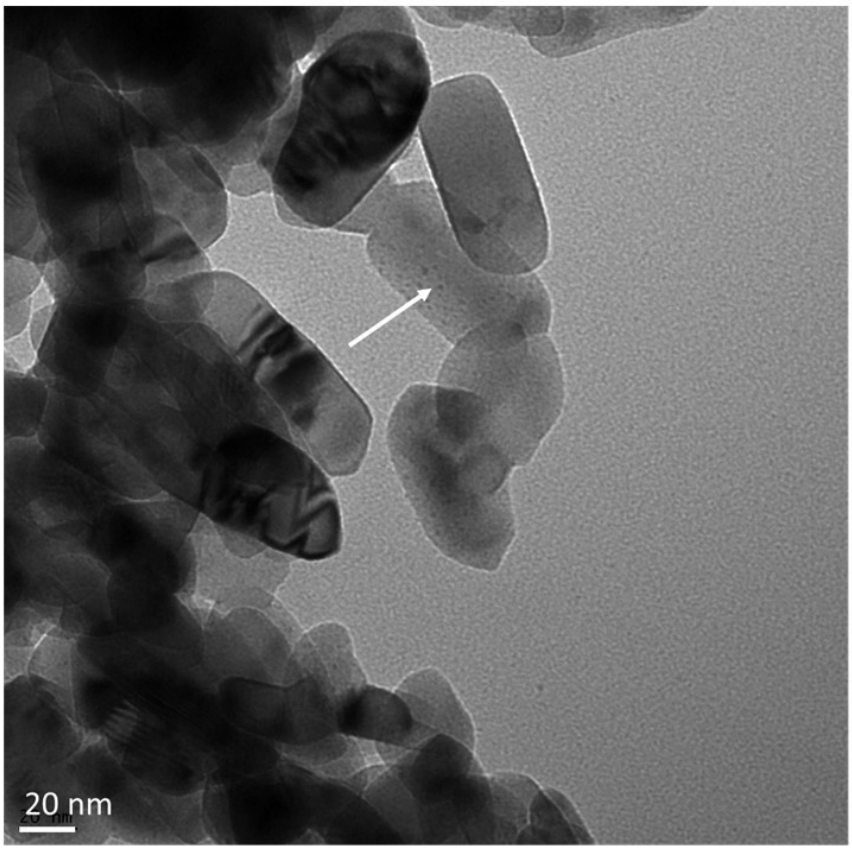


**Figure S6.** $nTiO_2$ stored in water with 500 μM $Ag^+$ at 40 °C for 4h. AgNPs on the $TiO_2$ surface are indicated by the white arrow.

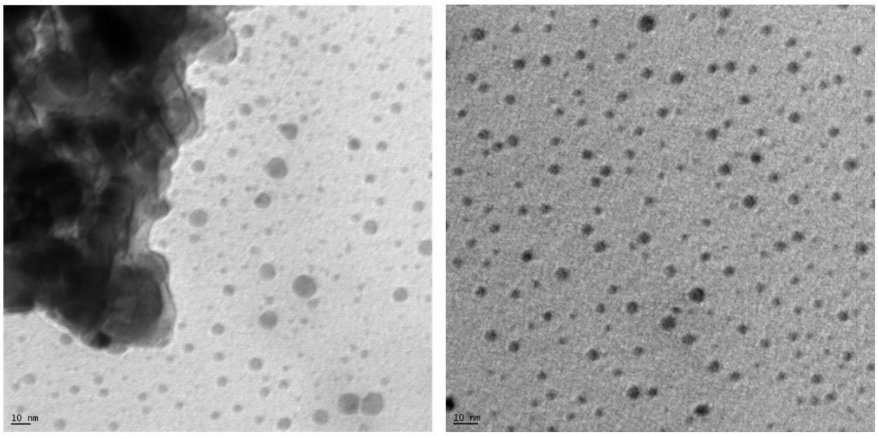


**Figure S7.** STEM images showing freely dispersed AgNPs in the vicinity of $nTiO_2$ stored within the presence of 500 μM $Ag^+$ for 4 hours at 40 °C. (Scale bars = 10 nm)

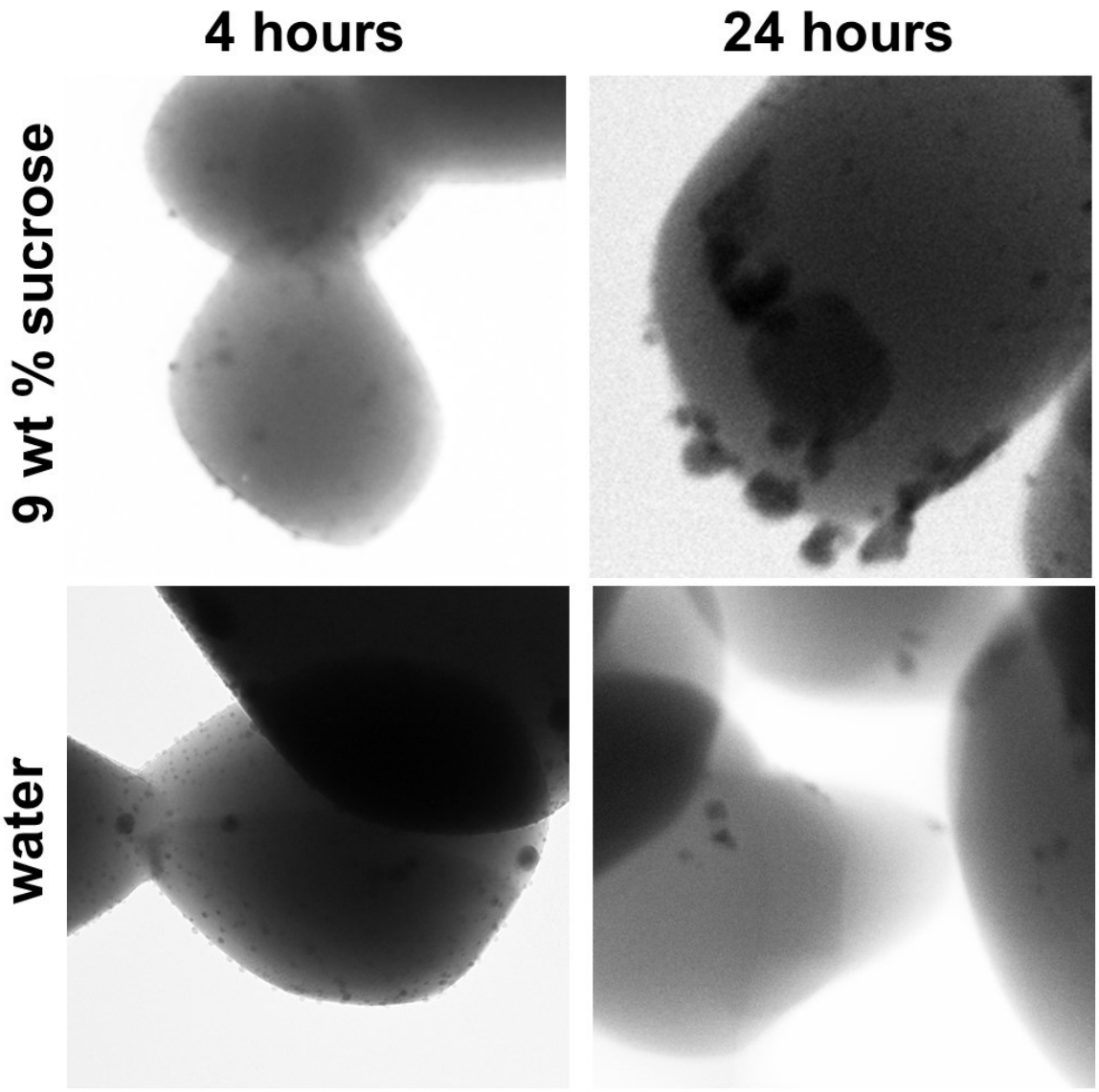


**Figure S8.** Representative STEM images of μ$TiO_2$ stored with 500 mM $Ag^+$ in 9 wt % sucrose solution (top) and water (bottom) for 4 hrs (left) and 24 hrs (right) at 40 °C. Note the disappearance of a large portion of the ultrasmall seed AgNPs on the surface of $TiO_2$ stored in water between 4 h and 24 h, whereas over the same time surface-bound ultrasmall AgNPs have persisted and in many cases grown on the surfaces of $TiO_2$ stored with sucrose. Each image represents an approximate area of 500 nm by 500 nm.

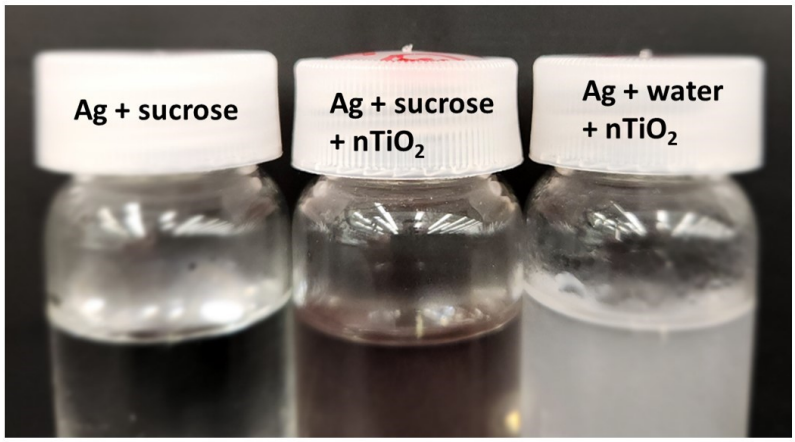


**Figure S9.** Close-up photograph of select vials similar to those depicted in **Figure 2**. Note the bloating of the vial cap only when sucrose and $nTiO_2$ are both present, signifying $CO_2$ production consistent with sucrose photodegradation by $TiO_2$. Similar effects were noted for $\mu TiO_2$. This photograph was taken after storage 4 days at 40 °C.

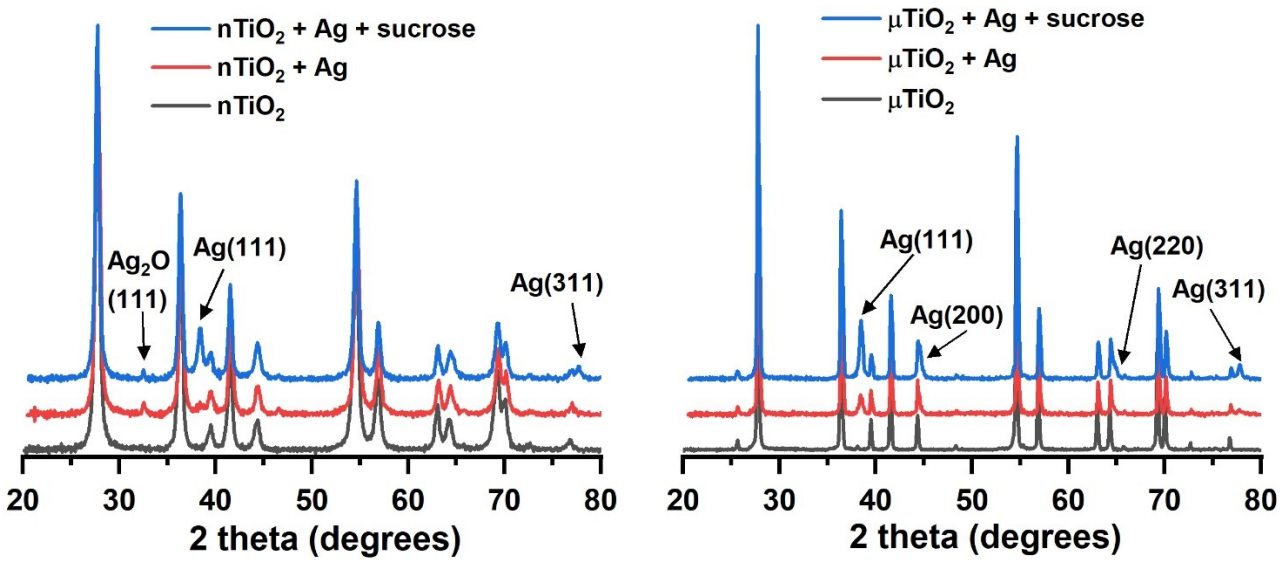


**Figure S10.** X-ray diffractograms of pristine $TiO_2$ (black), $TiO_2$ after exposure to 500 μM $Ag^+$ in water (red) and $TiO_2$ after exposure to 500 μM $Ag^+$ in 9 wt % sucrose solution (blue) for 10 days at 40 °C. Experiments with $nTiO_2$ and $\mu TiO_2$ are shown in the left and right panels, respectively. These data are identical to those in **Figure 2** of the main text except the diffractograms here are present over a larger range of scattering angles.

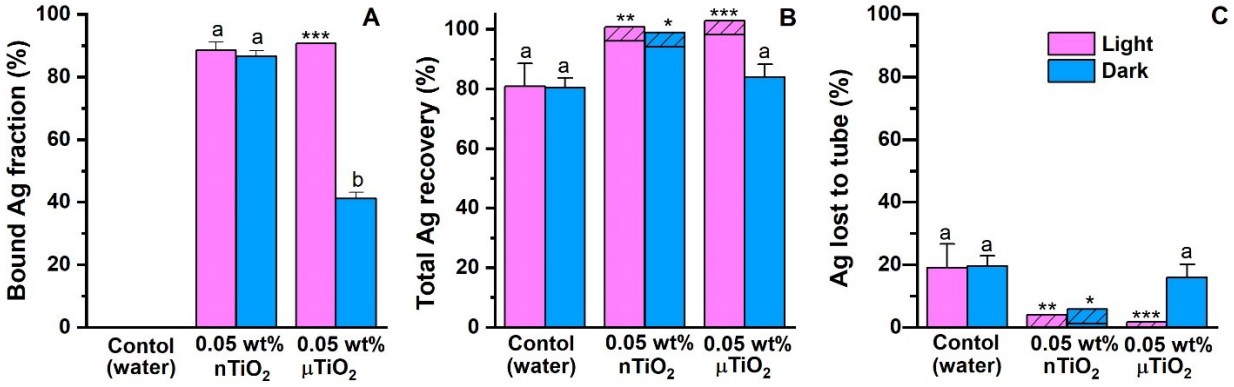


**Figure S11**. (A) Fraction of Ag bound to $TiO_2$ after 0.25 µg/L $Ag^+$ and either 0.05 wt% $nTiO_2$ or $\mu TiO_2$ were stored together in water for 1 day at 40 °C under ambient light and dark conditions. The control sample lacked $TiO_2$ ($Ag^+$ in water only). (B) Total recovery of the 0.25 µg/L $Ag^+$ initially added to each sample. Total recovery is the amount of Ag bound to $TiO_2$ (panel A) plus the amount of Ag remaining in the supernatant (**Figure 4A**, unbound Ag), divided by the total Ag initially added to the dispersion. (C) % of the total Ag lost to the container surface, determined as the difference between 100% and the total Ag recoveries plotted in panel (B). All bar heights represent average values over three replicates and error bars represent standard deviations from the mean. Bars indicated by different letters belong to statistically different groups ($p < 0.05$). Single asterisks represent samples in which all three replicates from the supernatant analysis had Ag concentrations below the LOD. Double asterisks represent samples in which at least one replicate was above the LOD but below the LOQ. In these cases, the hashed regions delineate maximum and minimum potential mean Ag content, as determined from the LOD and LOQ limits. The sample marked with a triple asterisk (0.05 wt % $\mu TiO_2$) had only one successful replicate for the precipitate analysis due to human error. Although we believe this sample likely belongs in group "a" (panel A) given the complimentary supernatant analysis (**Figure 4**), we were unable to perform a quantitative statistical analysis between this sample group and any other sample group.

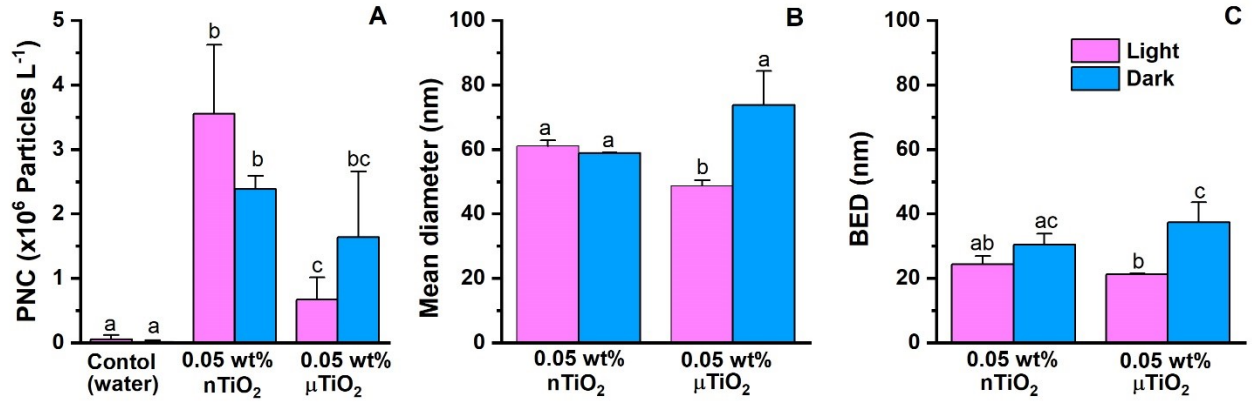


**Figure S12.** Particle number concentrations (PNCs) (A), mean diameters (B), and background equivalent diameters (BEDs) (C) of AgNPs in the supernatant after 0.25 μg/L $Ag^+$ and either 0.05 wt% $nTiO_2$ or $\mu TiO_2$ were stored together in water for 1 day at 40 °C under ambient light and dark conditions, as determined by SP-ICP-MS. All bar heights represent average values over three independent replicates and error bars represent standard deviations from the mean. Bars indicated by different letters belong to statistically different groups ($p < 0.05$). Note that we regard comparisons between samples sets in panels (A) and (B) to be most valid when the BED values for these respective sample sets are statistically indistinguishable, as indicated by panel (C).

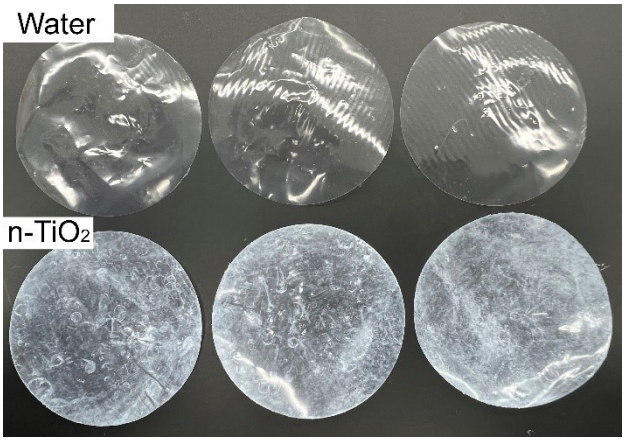


**Figure S13.** Photograph of AgNP/LDPE circles after attempting a migration test with water and $nTiO_2$. Note that strong adherence of $nTiO_2$ particles to the polymer surface. This behavior was not observed with $\mu TiO_2$.

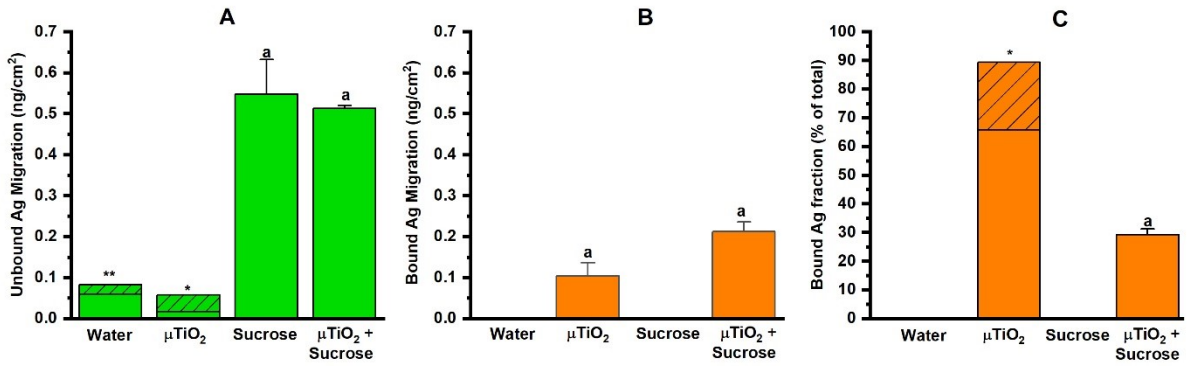


**Figure S14.** Speciation of Ag migrated from AgNP/LDPE sachets into simulants containing purified water, purified water and 0.01 wt % $\mu TiO_2$, purified water and 9 wt % sucrose, and purified water containing both 0.01 wt % $\mu TiO_2$ and 9 wt % sucrose. The storage time and temperature were 10 days and 40 °C. (A) and (B) show the total Ag in the supernatant (not bound to $\mu TiO_2$) and in the precipitate (bound to $\mu TiO_2$), respectively. (C) shows the calculated fraction of the total migrated A in the bound state, in wt %. All bar heights represent average values over 2-4 independent replicates and error bars represent standard deviations from the mean. Bars indicated by different letters belong to statistically different groups ($p < 0.05$). Single asterisks represent sample sets where all three replicates were above the LOD but below the LOQ; double asterisks represent sample sets where at least one replicate was below the LOQ but above the LOD. In these cases, hashed regions are used to indicate the range of potential Ag migration, as determined from LOD and LOQ limiting values.

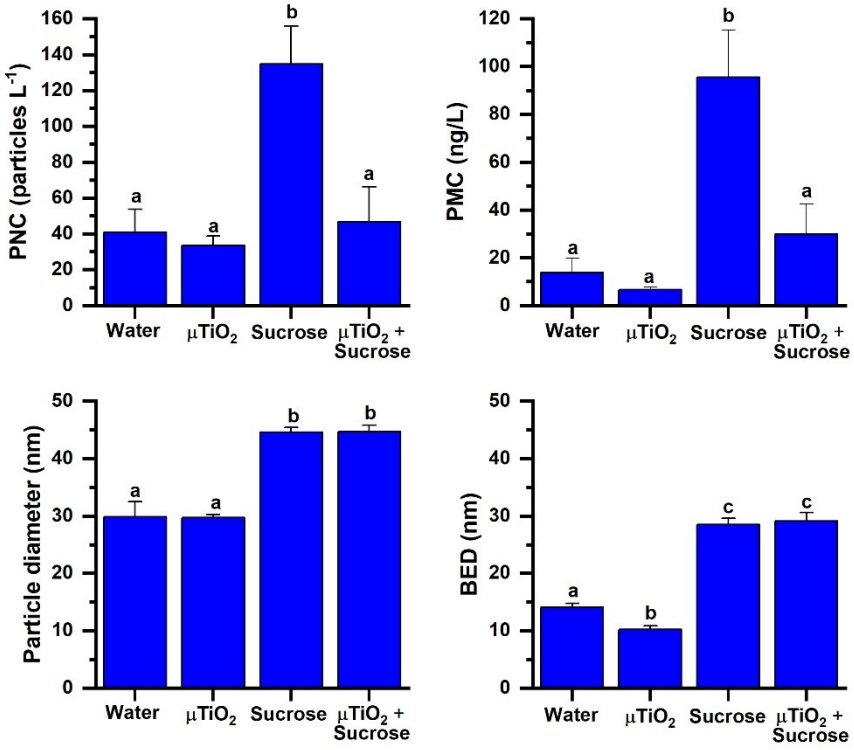


**Figure S15.** SP-ICP-MS analysis of Ag migrated from AgNP/LDPE sachets into simulants containing purified water, purified water and 0.01 wt % $\mu TiO_2$, purified water and 9 wt % sucrose, and purified water containing both 0.01 wt % $\mu TiO_2$ and 9 wt % sucrose. The storage time and temperature were 10 days and 40 °C. Particle number (PNCs) and mass (PMCs) concentrations are displayed in the top two panels. Mean particle diameters and background equivalent diameters (BEDs) are displayed in the bottom two panels. All bar heights represent average values over 2-4 independent replicates and error bars represent standard deviations from the mean. Bars indicated by different letters belong to statistically different groups ($p < 0.05$). Note that PNCs, PMCs, and particle diameters are dependent on BED values. Accordingly, we regard quantitative comparisons between samples sets to be most valid when the BED values for these respective sample sets are statistically indistinguishable.

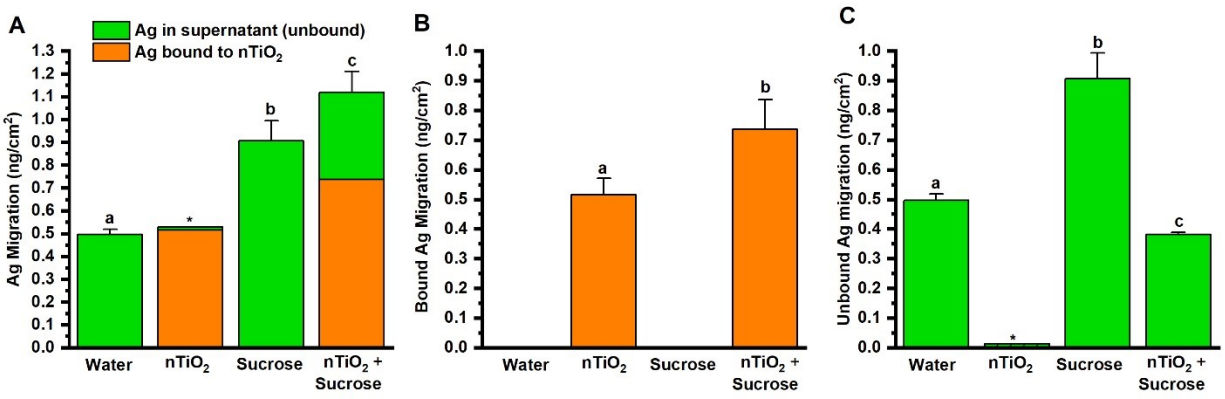


**Figure S16.** (A) Total Ag migration from AgNP/LDPE films (punched circles) into water, water containing 0.05 wt % $nTiO_2$, water containing 9 wt % sucrose, water containing 0.05 wt % $nTiO_2$ and 9 wt % sucrose, after 10 days at 40 °C. Portions of the total Ag bound to $nTiO_2$ (analysis of precipitate) and unbound in the supernatant are indicated. Direct comparisons of bound and unbound portions of migrated Ag are shown in (B) and (C), respectively. All bar heights represent mean values for 3 independent replicates and error bars represent standard deviations from the mean. Error bars in (A) pertain to the total migrated Ag and error bars in (B) and (C) pertain the highlighted component (bound or unbound). Letters above error bars indicate sample sets that belong to statistically different groups. Groups marked by an asterisk represent samples in which all replicates had measured concentrations in the supernatant below the LOD. In this case the hashed region indicates the maximum possible Ag migration determined by the LOD value. Note that the values for migrated Ag in a bound state (orange bars) are likely lower than the true values due to considerable loss of $nTiO_2$ to plastic surfaces.

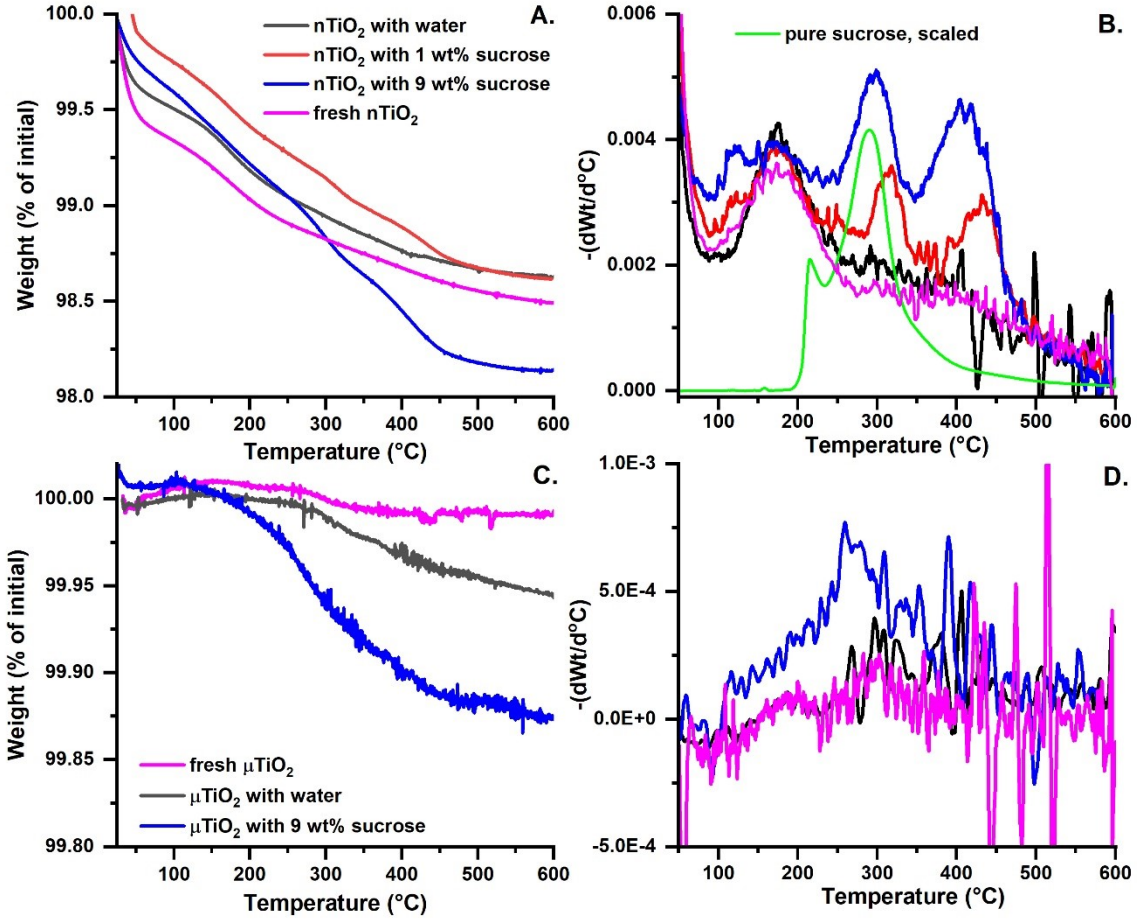


**Figure S17.** Thermogravimetric analysis of $nTiO_2$ (A, B) and $\mu TiO_2$ (C, D) after storage in purified water (black lines), 1% aqueous sucrose solution (red lines), or 9% aqueous sucrose solution (blue lines) for 24 h at 40 °C. Panels (A) and (C) show the % $TiO_2$ mass remaining as a function of temperature, and panels (B) and (D) show the derivative curves. Curves for fresh $TiO_2$ (magenta) and pure crystalline sucrose (green) are shown for comparison. The heating rate was 10 °C/min and all data shown were recorded under nitrogen atmosphere.

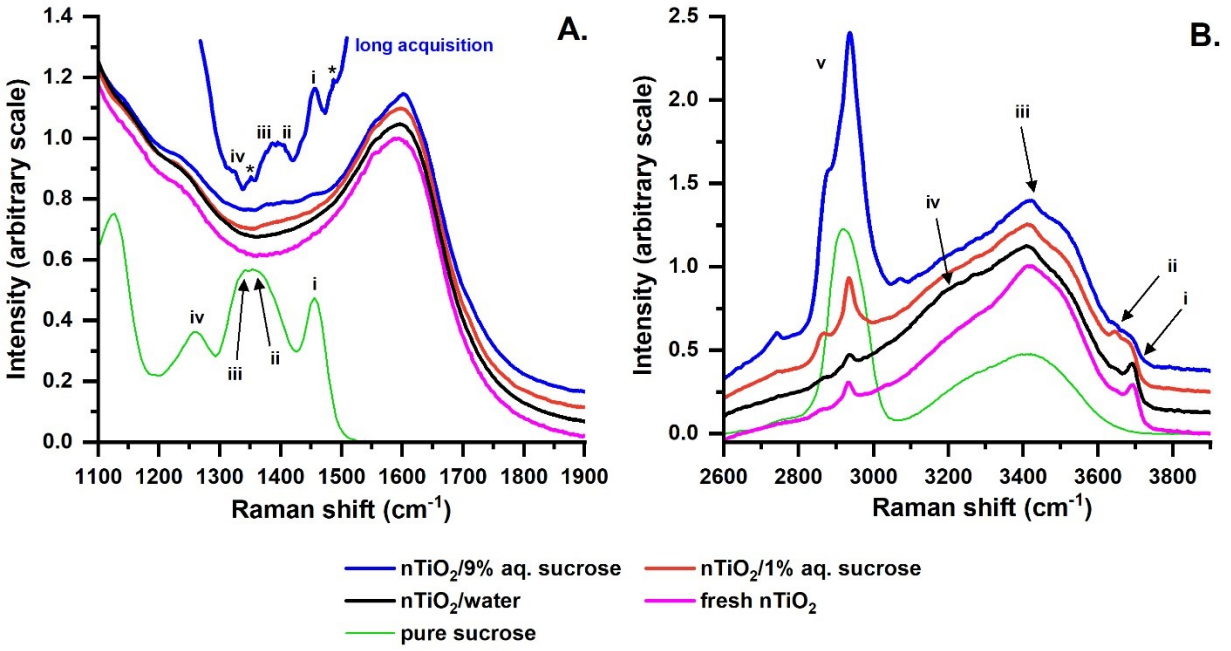


**Figure 18.** Raman scattering spectra of $nTiO_2$ after storage in purified water (blue), 1% aqueous sucrose solution (red) and 9 wt% aqueous sucrose solution (blue) for 24 h at 40 °C. Spectra of fresh $nTiO_2$ (pink) and hydrated sucrose (green, see experimental section) are also shown. Panels (A) and (B) highlight the $TiO_2$ OH bending (1100-1900 $cm^{-1}$) and stretching regions (2600-3900 $cm^{-1}$), respectively. The incident laser wavelength was 523 nm. Letters (i-v) and asterisks in each figure highlight peaks of interest that demonstrate the binding of sucrose to $nTiO_2$ (see discussion above). An expanded view of the 1300-1500 $cm^{-1}$ region for $nTiO_2$ stored in aqueous sucrose solution measured is also provided in panel (A). This region was captured with a longer exposure time to improve the spectral resolution of bound sucrose scattering peaks.

**References:**

(1) Yang, T.; Paulose, T.; Redan, B. W.; Mabon, J. C.; Duncan, T. V. Food and Beverage Ingredients Induce the Formation of Silver Nanoparticles in Products Stored within Nanotechnology-Enabled Packaging. *ACS Appl. Mater. Interfaces* **2021**, *13* (1), 1398-1412. DOI: 10.1021/acsami.0c17867.

(2) Qiaorun, Z.; Honghong, S.; Yao, L.; Bing, J.; Xiao, X.; Julian McClements, D.; Chongjiang, C.; Biao, Y. Investigation of the interactions between food plant carbohydrates and titanium dioxide nanoparticles. *Food Res. Int.* **2022**, *159*, 111574. DOI: https://doi.org/10.1016/j.foodres.2022.111574.

(3) Mathlouthi, M.; Vinh Luu, D. Laser-raman spectra of d-glucose and sucrose in aqueous solution. *Carbohydr. Res.* **1980**, *81* (2), 203-212. DOI: https://doi.org/10.1016/S0008-6215(00)85652-9.

(4) Wiercigroch, E.; Szafraniec, E.; Czamara, K.; Pacia, M. Z.; Majzner, K.; Kochan, K.; Kaczor, A.; Baranska, M.; Malek, K. Raman and infrared spectroscopy of carbohydrates: A review. *Spectrochim. Acta A* **2017**, *185*, 317-335. DOI: https://doi.org/10.1016/j.saa.2017.05.045.

(5) Bégin-Colin, S.; Gadalla, A.; Le Caër, G.; Humbert, O.; Thomas, F.; Barres, O.; Villiéras, F.; Toma, L. F.; Bertrand, G.; Zahraa, O.; et al. On the Origin of the Decay of the Photocatalytic Activity of TiO2 Powders Ground at High Energy. *J. Phys. Chem. C* **2009**, *113* (38), 16589-16602. DOI: 10.1021/jp900108a.

(6) Soria, J.; Sanz, J.; Sobrados, I.; Coronado, J. M.; Maira, A. J.; Hernández-Alonso, M. D.; Fresno, F. FTIR and NMR Study of the Adsorbed Water on Nanocrystalline Anatase. *J. Phys. Chem. C* **2007**, *111* (28), 10590-10596. DOI: 10.1021/jp071440g.

(7) Hosseinpour, S.; Tang, F.; Wang, F.; Livingstone, R. A.; Schlegel, S. J.; Ohto, T.; Bonn, M.; Nagata, Y.; Backus, E. H. G. Chemisorbed and Physisorbed Water at the TiO2/Water Interface. *J. Phys. Chem. Lett.* **2017**, *8* (10), 2195-2199. DOI: 10.1021/acs.jpclett.7b00564.

(8) Šćepanović, M.; Abramović, B.; Golubović, A.; Kler, S.; Grujić-Brojčin, M.; Dohčević-Mitrović, Z.; Babić, B.; Matović, B.; Popović, Z. V. Photocata/lytic degradation of metoprolol in water suspension of TiO2 nanopowders prepared using sol–gel route. *J. Sol-Gel Sci. Technol.* **2012**, *61* (2), 390-402. DOI: 10.1007/s10971-011-2639-9.

(9) Kim, G.; Lee, S.-H.; Choi, W. Glucose–TiO2 charge transfer complex-mediated photocatalysis under visible light. *Appl. Catal., B* **2015**, *162*, 463-469. DOI: https://doi.org/10.1016/j.apcatb.2014.07.027.